

Kekulé Moiré Superlattices

Yusen Ye¹, Jimin Qian¹, Xiao-Wei Zhang¹, Chong Wang¹, Di Xiao^{1,2*}, Ting Cao^{1*}.

¹ Department of Materials Science and Engineering, University of Washington, Seattle, WA, USA

² Department of Physics, University of Washington, Seattle, WA, USA

* Corresponding Authors. Emails: dixiao@uw.edu, tingcao@uw.edu.

Abstract

Moiré superlattices from stacks of van der Waals materials offer an exciting arena in the fields of condensed matter physics and materials science. Typically, these moiré superlattices consist of materials with identical or similar structures, and the long moiré period arises from a small twist angle or lattice mismatch. In this article, we discuss that long moiré period appears in a new moiré system by stacking two dissimilar van der Waals layers with large lattice mismatch, resulting in couplings between moiré bands from remote valleys in the momentum space. In this system, the first layer is reconstructed using a $\sqrt{3}$ by $\sqrt{3}$ supercell that resembles the Kekulé distortion in graphene, and such reconstruction becomes nearly commensurate with the second layer. This Kekulé moiré superlattice is realized in heterostructures of transition metal dichalcogenides and metal phosphorus trichalcogenides such as MoTe₂/MnPSe₃. By first-principles calculations, we demonstrate that the antiferromagnetic MnPSe₃ strongly couples the otherwise degenerate Kramers' valleys of MoTe₂, resulting in valley pseudospin textures that depend on Néel vector direction, stacking geometry, and external fields. With one hole per moiré supercell, we predict that the system can become a Chern insulator, of which the topology is tunable by external fields.

1 Introduction

Moiré superlattices are usually formed by stacking van der Waals (vdW) materials with a small twist angle and/or a small lattice mismatch. The nearby electronic states in the momentum \mathbf{k} -space are coupled by the long moiré period and, in the case of graphene and transition metal dichalcogenides, resulting in two independent copies of moiré bands from each valley [1–5]. These moiré bands, combined with spin degrees of freedom as in a TMD moiré bilayers, can bring about a variety of correlated and topological phases[6–13]. However, the short-range nature of the moiré scattering potential, together with the valley-spin locking effect, prevents direct coupling between the two Kramers' valleys (i.e., $|\mathbf{K}, \uparrow\rangle$ and $|\mathbf{K}', \downarrow\rangle$) from the same layer[14]. Since the moiré effects modulate these valleys independently, it remains challenging to fully control and utilize the Kramers' valley-spin pairs within the moiré platform.

Prior attempts to connect remote valleys have focused on correlation effects and lattice reconstruction. On the one hand, the correlation effects have the potential to induce a coherent superposition between valley states, but controlling the strength and the form of correlation is challenging for the Kramers' valley-spin pairs. On the other hand, direct intervalley coupling can be accomplished by \mathbf{k} -space scattering on the scale of the large reciprocal lattice vector in a structure without moiré effects. For example, in Kekulé distorted graphene, the $\sqrt{3} \times \sqrt{3}$ reconstruction of the unit cell generates scattering potential that connects \mathbf{K} and

\mathbf{K}' , giving rise to intervalley coherent states [15–18]. Kekulé graphene has been achieved experimentally through the use of adatoms to form an effective $\sqrt{3} \times \sqrt{3}$ lattice [15, 19], or by stabilizing a Kekulé bond-ordered graphene through interaction when Landau levels appear under high magnetic field [20, 21]. However, as the Kekulé reconstruction in graphene relies on structure modifications and electron correlations, rational control of the intervalley scattering at the moiré periodicity remain challenging. It is also a non-trivial task to extend the Kekulé effects to other moiré systems and establish a tunable coupling in a Kramers' valley-spin pair to navigate the fascinating moiré space.

In this article, we discuss a new type of moiré system that goes beyond the limits of small twist angle and small lattice mismatch, and, in doing so, short-range and long-range scatterings in \mathbf{k} -space emerge spontaneously and simultaneously. By first-principles calculations and continuum modeling, we show that the coupling between Kramers' valley-spin states induces a pseudospin topological texture at the moiré scale in $\text{MoTe}_2/\text{MnPSe}_3$ superlattices. We show that the coupling and the topological texture can be fully controlled by magnetic order and external fields, leading to topologically non-trivial bands and a quantum anomalous Hall insulator phase at one hole per moiré cell.

2 Results and Discussion

2.1 Kekulé Moiré Structure and Intervalley Coupling

The new moiré superlattice consists of two distinct layers of two-dimensional (2D) hexagonal lattices. The ratio between their lattice constants, a_L/a_S , is about $\sqrt{3}$. We then reconstruct a $\sqrt{3}a_S \times \sqrt{3}a_S$ Kekulé cell of the smaller lattice, such that the two layers become almost commensurate as shown in Fig. 1(a). We redefine the lattice mismatch to be measured between $\sqrt{3}a_S$ and a_L , and the twist angle to be measured starting from 30° . This construction, which we coin the name as Kekulé moiré superlattices, can be achieved by combining any pair of layered vdW materials equipped with a hexagonal Bravais lattice, as long as their lattice constant ratio is about $\sqrt{3}$. As this work aims to couple and control the Kramers' valley-spin pairs, we choose the first layer with a_S to be TMD, which has been known for their valley-spin degrees of freedom [22, 23]. However, even with a spin-conserving Umklapp scattering from the lattice potential of the second layer, which folds both \mathbf{K}_{TMD} and \mathbf{K}'_{TMD} back to Γ , the spin-valley locking effect will forbid any coupling between $|\mathbf{K}, \uparrow\rangle$ and $|\mathbf{K}', \downarrow\rangle$. As a result, the heterostructure will not develop any intervalley coupling if a spin-flipping mechanism, e.g., magnetism or spin-orbit coupling, is not involved. Fortunately, a class of magnetic vdW materials, metal phosphorus trichalcogenides (MPX_3), has lattice constants approximately matching $\sqrt{3}a_{\text{TMD}}$, and is therefore used as the second layer. As an important class of vdW materials, MPX_3 has rich magnetic orders, including ferromagnetic (FM), zigzag anti-ferromagnetic (AFM), and Néel AFM depending on the atomic species of M and X [24, 25]. Based on optimal lattice matching conditions, several combinations of TMD and MPX_3 that can give rise to long moiré period are listed in Table 1.

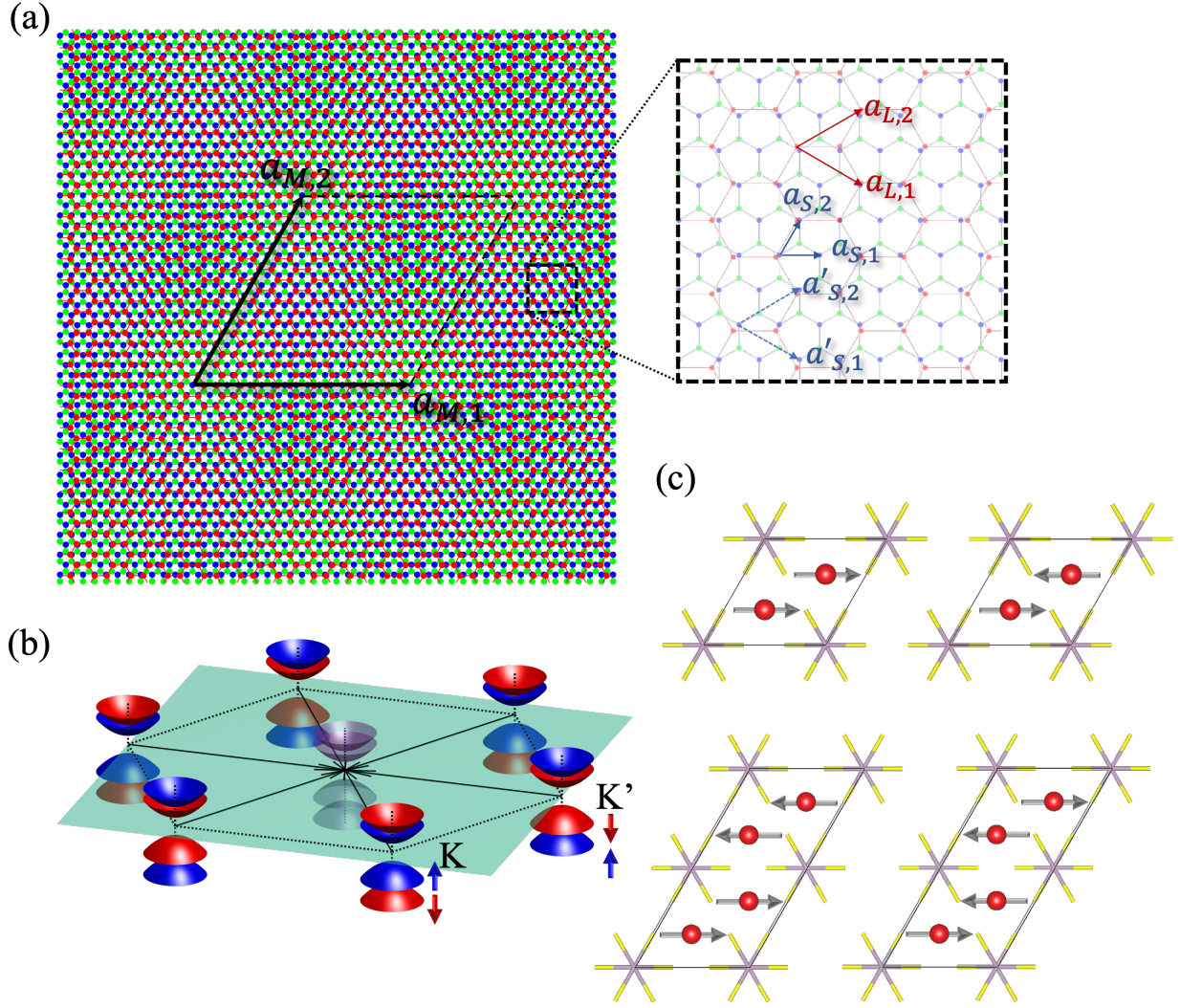


Figure 1: (a) The moiré pattern formed by stacking MPX_3 on top of TMD with a 30° twist angle. Blue (red) circles represent the metal ions in TMD (MPX_3). Inset: $\{\mathbf{a}_S\}$ ($\{\mathbf{a}_L\}$) denote the primitive lattice vectors of TMD (MPX_3), where $\sqrt{3}\|\mathbf{a}_S\| \approx \|\mathbf{a}_L\|$ as shown in dashed $\{\mathbf{a}'_S\}$. (b) A schematic plot of monolayer TMD band structure showing the valleys. The \mathbf{K} (\mathbf{K}') valleys of monolayer TMD are locked with spin up (down) as indicated by blue (red) coloring. Under Kekulé reconstruction, both valleys are folded back to Γ . (c) Possible magnetic orders of MPX_3 are shown. Arrows denote local magnetic moments. From upper left going clockwise: FM, AFM Néel, AFM stripy, AFM zigzag.

The effective potential of MPX_3 that acts on TMD can be expanded as

$$V(\mathbf{r}) = \sum_{\mathbf{G}_L} e^{i\mathbf{G}_L \cdot \mathbf{r}} \mathbf{V}_{\mathbf{G}_L} \cdot \boldsymbol{\sigma},$$

where \mathbf{G}_L is a reciprocal lattice vector of MPX_3 , $\mathbf{V}_{\mathbf{G}_L} \equiv (V_{0,\mathbf{G}_L}, V_{x,\mathbf{G}_L}, V_{y,\mathbf{G}_L}, V_{z,\mathbf{G}_L})$ is the Fourier transformed lattice potential in a four-vector form to denote the spin-independent and spin-dependent components, and $\boldsymbol{\sigma} \equiv (\sigma_0, \sigma_x, \sigma_y, \sigma_z)$ is a four vector formed by \mathbb{I}_2 and Pauli matrices which act on the spinor Hilbert space. To this end, many previous works have studied the proximity effects of a magnetically ordered vdW material layered on TMD, but these efforts have mostly used the simple analog of homogeneous magnetic field, i.e., $\mathbf{V}_{\mathbf{G}_L} \cdot \boldsymbol{\sigma}$ at $\mathbf{G}_L = 0$ [26–30]. In Kekulé moiré superlattice, to couple the two valleys in both momentum and spinor space, we need a lattice scattering momentum $\mathbf{G}_L = \pm(\mathbf{K} - \mathbf{K}')$, as well as a

spin-flipping matrix σ_x or σ_y . Combined together, the condition is $V_{x/y,\pm(\mathbf{K}-\mathbf{K}')} \neq 0$. This requires an in-plane magnetic order in MPX₃, as a sizeable V_{x,\mathbf{G}_L} or V_{y,\mathbf{G}_L} can be obtained from Fourier transforming an effective exchange field that originates from spin polarization aligned in-plane. Further, a more detailed symmetry analysis (see appendix) shows that only FM and Néel ordered AFM can generate an intervalley coupling. Based on this phenomenological theory, we select MoTe₂ and MnPSe₃ (in-plane AFM ordered) from Table 1 to illustrate the Kekulé moiré physics in a realistic heterostructure.

	MnPS ₃	MnPSe ₃	FePS ₃	CoPS ₃	NiPS ₃	NiPSe ₃
a(Å)	6.08	6.38	5.94	5.91	5.82	6.13
MO[31–34]	Néel(z)	Néel(xy)	zigzag(z)	zigzag(x)	zigzag(x)	zigzag(x)
TMD match	MoTe ₂	MoTe ₂	MoTe ₂ , WSe ₂	MoSe ₂ , WSe ₂	MoSe ₂ , WSe ₂	MoTe ₂

Table 1: Lattice constant, ground state magnetic order (MO) and best lattice-matching TMDs. (Lattice constants are obtained from DFT)

2.2 MoTe₂/MnPSe₃ Heterostructure

In the MoTe₂/MnPSe₃ heterostructure, the lattice mismatch is about 4%. The resulting moiré wavelength can be as large as 8 nm, given by a_{MoTe_2}/δ , where $\delta = \frac{|a_{\text{MnPSe}_3} - \sqrt{3}a_{\text{MoTe}_2}|}{a_{\text{MnPSe}_3}}$ (see appendix). The moiré lattice vectors align with the primitive lattice vectors of MoTe₂ as illustrated schematically in Fig.1(a). Similar to TMD bilayers that can be either R-type or H-type, the Kekulé moiré heterostructure can also be constructed from either 0° or 60° twist angle (measured from 30°). The two constructions are the same up to a total rotation if either layer is inversion symmetric; if both layers break inversion symmetry, the 0° and 60° constructions are of different structures and thus will host different electronic behaviors in general. Since the lattice of MnPSe₃ contains inversion symmetry, the 0° and 60° constructions are equivalent in the MoTe₂/MnPSe₃ heterostructure.

To study the MoTe₂/MnPSe₃ Kekulé moiré superlattice that consists of over 3000 atoms in one moiré supercell, we performed first-principles calculations (see appendix) on 12×12 commensurate structures based on local stacking geometry, followed by continuum modeling using parameters from the calculations. Among these commensurate unit cells are three high-symmetry stackings shown in Fig. 2(c). The DFT-PBE band structure of stacking A shows a type-II band alignment in Fig.2(b). At Γ , the band edge states are formed by MoTe₂, and the \mathbf{K} and \mathbf{K}' valleys are folded to the center of the Kekulé Brillouin zone by the Umklapp scattering. As the valence band top from MoTe₂ is well separated from the MnPSe₃ bands located at 0.66 eV below, the two topmost valence bands become ideal candidates to analyze and control intervalley coupling in the Kekulé moiré superlattice. The band alignments in other commensurate stacking geometries are generally similar to Fig.2(c) except for band splittings and energy variations on the order of tens of meV, which arise from the intervalley coupling and intravalley potential that we will discuss next.

2.3 Moiré Hamiltonian and Pseudospin Texture

In the Kekulé moiré superlattice, the valley-spin polarized Bloch states of MoTe₂, i.e., $\{|\mathbf{K}, \uparrow\rangle, |\mathbf{K}', \downarrow\rangle\}$, are mapped to $\pm\kappa$ in the moiré Brillouin zone (Fig.3(b)). We thus use

an effective moiré Hamiltonian in the basis of $|\mathbf{k} \mp \boldsymbol{\kappa}\rangle$ to describe the low-energy physics of the moiré valence bands:

$$H_{\text{eff}}(\mathbf{r}) = \begin{bmatrix} H_{\mathbf{k}-\boldsymbol{\kappa}} + V_d(\mathbf{r}) & \Delta_{\text{int}}(\mathbf{r}) \\ \Delta_{\text{int}}^\dagger(\mathbf{r}) & H_{\mathbf{k}+\boldsymbol{\kappa}} + V_d(\mathbf{r}) \end{bmatrix}. \quad (1)$$

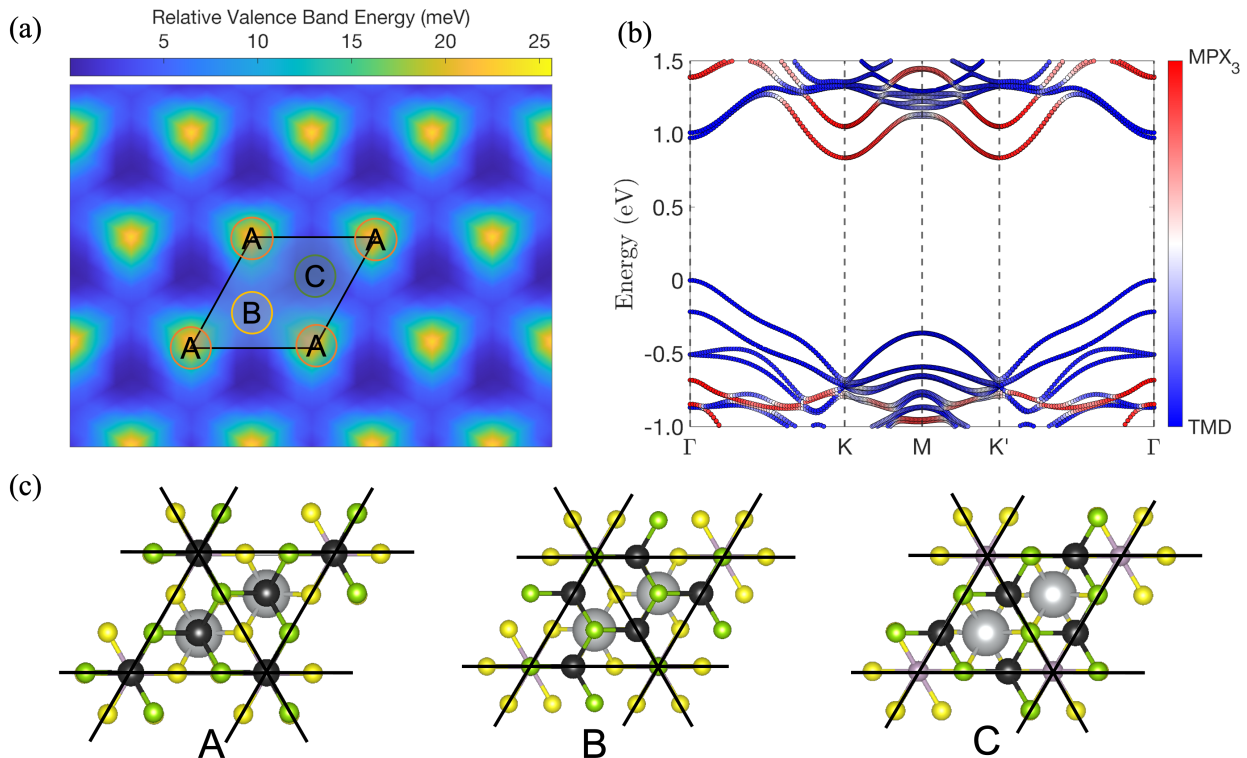


Figure 2: (a) Kohn-Sham DFT valence band edge energies in the MoTe₂/MnPSe₃ moiré superlattice. A,B,C are high symmetry stacking regions that are shown in (c). (b) Kohn-Sham DFT bandstructure of MoTe₂/MnPSe₃ at high-symmetry stacking A. Blue (red) shows the projection of bands to the MoTe₂ (MnPSe₃) orbitals. (c) Three high symmetry stackings of TMD/MPX₃ heterostructure in top view. There exists mirror symmetries, σ_V , in every high symmetry local structure illustrated by the black solid lines. Black and green spheres illustrate transition metal and chalcogen atoms in the TMD layer, respectively; silver, yellow, and light purple spheres illustrate transition metal, chalcogen, and phosphorus atoms in MPX₃ layer, respectively.

We use the effective mass approximation: $H_{\mathbf{k}\mp\boldsymbol{\kappa}} = -\frac{\hbar^2(\mathbf{k}\mp\boldsymbol{\kappa})^2}{2m^*}$, where $m^* = 0.86m_e$ from first-principles calculations. $V_d(\mathbf{r})$ depicts the intravalley moiré potential, which reads[3, 5]:

$$V_d(\mathbf{r}) = 2V \sum_{j=1,3,5} \cos(\mathbf{g}_{M,j} \cdot \mathbf{r} + \psi), \quad (2)$$

where V is the structural potential amplitude, $\mathbf{g}_{M,j}$ are $(j-1)\pi/3$ counter-clockwise rotated from $\frac{4\pi}{\sqrt{3}L_M}\hat{y}$, and ψ is a phase factor parameter. V and ψ can be obtained by fitting to the energy of valence band maxima in the 12×12 commensurate stackings, using the first-principles results in Fig.2(a). We find $V = 2.3$ meV and $\psi = -16.6^\circ$.

$\Delta_{\text{int}}(\mathbf{r})$ describes the coupling between the Kramers' valleys in the same layer, which is a virtual process that would have been absent without the Kekulé moiré effects. We note that

similar forms of the Hamiltonian have appeared in previous studies in TMD moiré structures, but the off-diagonal terms represent a real scattering process from a valley in one layer to an adjacent valley in the other layer[3, 4, 35]. The amplitude of Δ_{int} can be obtained directly from the first-principles calculations, which equals to half of the splitting between the top two valence bands in commensurate heterostructures shown in Fig.3(a). We find maximum band splitting of 3.0 meV in the region between A and B, but the splitting vanishes at the three high-symmetry stackings. To understand this pattern, we notice that all the three high-symmetry structures contain lattice mirror symmetries as shown in Fig.2(c). In the cases that the Néel vectors are in the mirror planes, degeneracy between the $|\mathbf{K} \uparrow\rangle$ and $|\mathbf{K}' \downarrow\rangle$ valleys is protected. If the Néel vector rotates away, the lattice mirror symmetries still forbid intervalley coupling in the orbital parts of wavefunction, as long as the spin-orbit term in the interlayer coupling Hamiltonian is weak. This analysis has also been confirmed by our DFT calculations.

Equation (1) suggests that Δ_{int} can be recognized as a pseudospin magnetic field acting on the valley pseudospin as $\Delta_{\text{int}} = \Re(\Delta_{\text{int}})\tau_x - \Im(\Delta_{\text{int}})\tau_y$, where τ 's are the Pauli matrices. As a result, Δ_{int} not only carries an amplitude corresponding to the size of the pseudospin magnetic field, but also a phase related to the direction of this field in the 2D plane. Therefore, highly interesting valley pseudospin textures has appeared in the moiré supercell as shown in Fig.3(a).

In MoTe₂/MnPSe₃ Kekulé moiré superlattices, $\Delta_{\text{int}}(\mathbf{r})$ can be approximated in the first few harmonic expansions by noticing the translational symmetry and $\hat{\mathcal{C}}_3$ rotational symmetry[3, 4]. Furthermore, as $\Delta_{\text{int}}(\mathbf{r})$ vanishes at the high symmetry stackings, the approximate form requires at least the first two harmonic expansions, which reads

$$\begin{aligned} \Delta_{\text{int}}(\mathbf{r}) = & \Delta(1 + \omega e^{-i(\mathbf{g}_{M,1}\cdot\mathbf{r})} + \omega^2 e^{-i\mathbf{g}_{M,2}\cdot\mathbf{r}}) \\ & - \Delta(e^{-i(\mathbf{g}_{M,1}+\mathbf{g}_{M,2})\cdot\mathbf{r}} + \omega e^{-i(\mathbf{g}_{M,3}\cdot\mathbf{r})} + \omega^2 e^{-i\mathbf{g}_{M,6}\cdot\mathbf{r}}). \end{aligned} \quad (3)$$

Here, $\omega = \langle \mathbf{K}, \uparrow | \hat{\mathcal{C}}_3^{-1}(\mathbf{K}, \uparrow) \rangle \langle \mathbf{K}', \downarrow | \hat{\mathcal{C}}_3(\mathbf{K}', \downarrow) \rangle = e^{i4\pi/3}$. The phase factor is obtained from both the orbital and the spinor part of the valley states[4]. As $|\pm\mathbf{K}\rangle$ mainly consists of $|d_{x^2-y^2}\rangle \pm i|d_{xy}\rangle$ orbitals from the Mo ions, applying the $\hat{\mathcal{C}}_3$ results in an orbital phase factor of $\exp(\pm i2\pi/3)$. Besides, the $|\pm\mathbf{K}\rangle$ valleys are spin-up(down) from the valley-spin locking, which generates an extra factor of $\exp(\mp i\pi/3)$. The effect of $\hat{\mathcal{C}}_3$ on the Bloch phases from $|\pm\mathbf{K}\rangle$ are canceled out by the same but opposite phase from the momentum carried by Δ_{int} . These together produce the overall phase of $\omega = e^{i4\pi/3}$. Fitting equation (3) to DFT calculations, we find $\Delta = -0.35$ meV.

The valley pseudospin textures of a Kekulé moiré superlattice lead to winding patterns of spin polarization in the moiré frontier orbitals. At the conduction band edge where $|\mathbf{K}, \uparrow\rangle$ and $|\mathbf{K}', \downarrow\rangle$ share the same orbital wavefunction of $|d_{z^2}\rangle$ but differ in their spins, Δ_{int} represents a real-space magnetic field that dictates noncollinear spin orientations of Kekulé cells. At the valence band edge where the two valleys carry different orbitals and spins, Δ_{int} represents a set of magnetic field acting on each orbital-spin basis. As such the frontier orbital carries entangled orbitals and spins at the moiré periodicity.

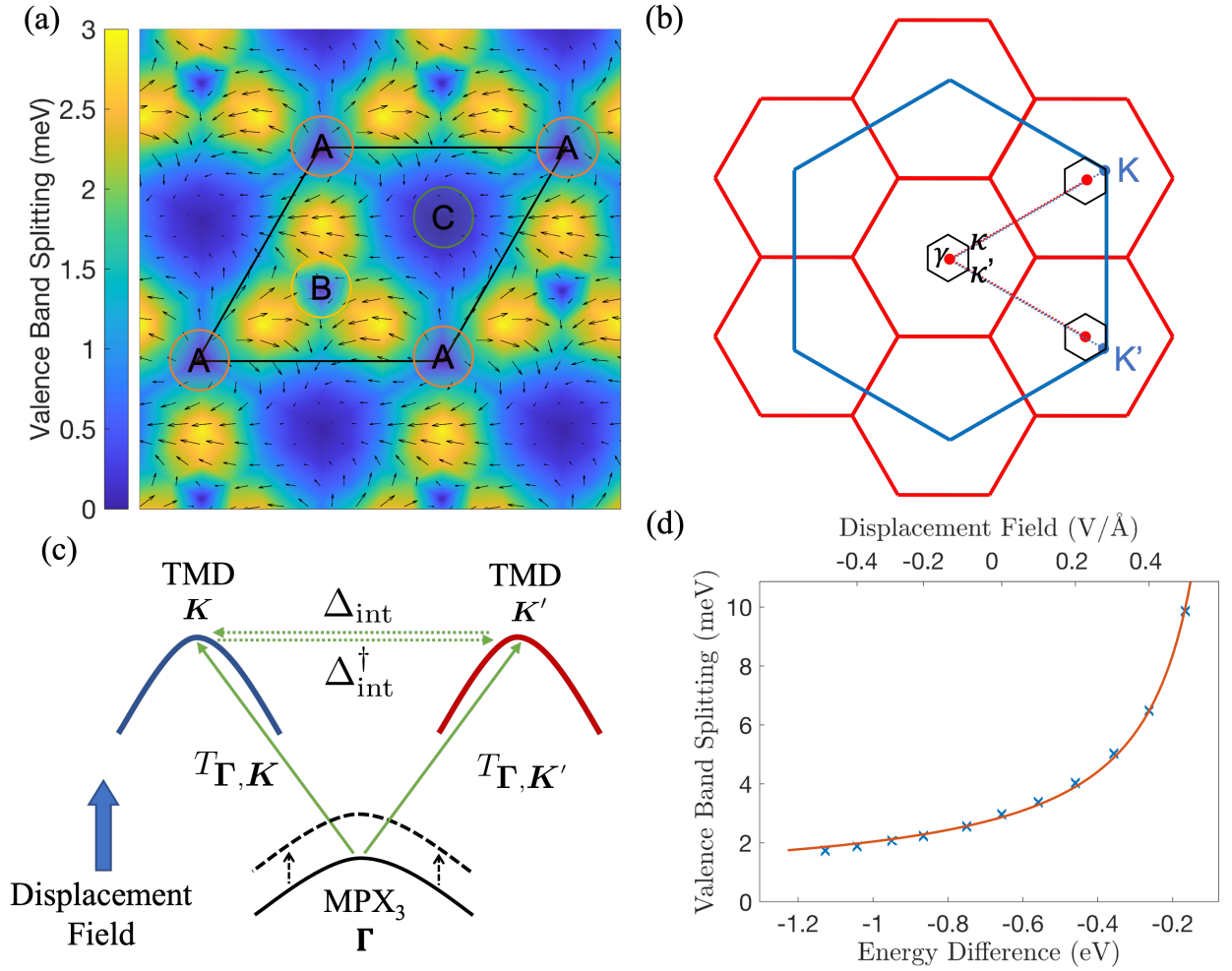


Figure 3: (a) Intervalley coupling induced splitting between MoTe₂ valence bands in the real-space MoTe₂/MnPSe₃ moiré superlattice from first-principles calculation on a 12×12 grid. The deep blue color shows no intervalley splitting while the yellow color shows largest intervalley splitting up to 3.0 meV. Arrows represent the strength and the direction of effective valley pseudospin magnetic field from model as defined in the main text. (b) The formation of moiré Brillouin zone. The reciprocal lattice vectors of MPX₃ (red) fold the K/K' points back around Γ point as κ/κ' points. The resulting moiré Brillouin zone is parallel to the TMD (blue) Brillouin zone. (c) Schematic physical origin of the intervalley coupling (green dashed line) mediated by the magnetic substrate, through a two-step hopping (green solid lines) between $|K\rangle$ and $|K'\rangle$ valence valleys of TMD. Dashed parabolas represent bands being pushed up by an out-of-plane displacement field shown as the large blue arrow, which enlarges the intervalley coupling. (d) Valley splitting inversely proportionate to the energy difference between $|K, \text{MoTe}_2\rangle$ and $|\Gamma, \text{MnPSe}_3\rangle$ bands, where the energy difference is tuned by the out-of-plane displacement field as shown in the top x -axis. Crosses and the line are from first-principles results and fitting, respectively. In the fitting, we find $y = -\frac{1.58}{x} + 0.46$, where y is the valence band splitting, and x is the energy difference between relevant bands from MoTe₂ and MnPSe₃.

2.4 Controlling Pseudospin and Band Topology

The Kekulé moiré Hamiltonian and the valley pseudospin textures can be controlled by electric field and magnetic order. In our calculations, we apply an out-of-plane displacement field

to the MoTe₂/MnPSe₃ heterostructure with 0.1 eV/Å increment. The amplitude of Δ_{int} (and effectively Δ as from equation (3)) increases dramatically under larger electric field pointing from the MPX₃ to TMD. At the stacking region with maximum valley splitting, Δ_{int} increases from 3.0 meV at no electric field to 5.0 meV at +0.3 V/Å electric field (Fig.3(d)). To understand why electric field strongly couples to the pseudospin magnetic field strength, we analyze the microscopic interaction that leads to Δ_{int} . In vdW heterostructures, electrons can hop between layers while conserving the in-plane \mathbf{k} . In TMD/MPX₃ Kekulé moiré, $|\pm\mathbf{K}, \text{TMD}\rangle$ directly couples to $|\Gamma, \text{MPX}_3\rangle$. We denote this hopping process as $T_{\Gamma, \pm\mathbf{K}}$. The coupling between $|\pm\mathbf{K}, \text{TMD}\rangle$ can be then captured by a two-step hopping, $T_{\Gamma, \pm\mathbf{K}}T_{\Gamma, \mp\mathbf{K}}^\dagger$, mediated by MPX₃ as shown in Fig.3(c). We can apply second order perturbation theory to obtain $\Delta_{\text{int}} = \frac{1}{2}T_{\Gamma, \mathbf{K}}^\dagger T_{\Gamma, \mathbf{K}'} \left(\frac{1}{E_{\mathbf{K}} - E_{\Gamma, \text{MPX}_3}} + \frac{1}{E_{\mathbf{K}'} - E_{\Gamma, \text{MPX}_3}} \right)$ (see appendix). This analysis agrees well with our first-principles calculations, in which Δ_{int} is indeed inversely proportional to the energy difference between $|\mathbf{K}, \text{TMD}\rangle$ and $|\Gamma, \text{MPX}_3\rangle$. In the MoTe₂/MnPSe₃ heterostructure, our fitting shows that the relevant $|\Gamma, \text{MnPSe}_3\rangle$ band is about 0.66 eV below the $|\pm\mathbf{K}, \text{MoTe}_2\rangle$ bands at zero displacement field, consistent with the band structure in Fig.2(b).

The global phase of the valley pseudospin texture is locked to the Néel vector of MPX₃. As the Néel vector is rotated from the +x axis (which is the direction of the Néel vector for prior calculations and modeling) counter-clockwise by θ , its effect to Δ_{int} can be analyzed from the spin dependence of the hopping channel, i.e., $T_{\Gamma, \mathbf{K}'} \propto \langle \chi | \downarrow \rangle$, where $|\chi\rangle$ is the spinor component of the relevant magnetic bands in MPX₃, and its direction is mostly collinear with the magnetic order. When the Néel vector is rotated by θ , the spinor inner product acquires a phase: $\langle U^{-1}(\theta)\chi | \downarrow \rangle = \langle \chi | U(\theta) \downarrow \rangle = \langle \chi | \downarrow \rangle e^{i\theta/2}$. Combined with the phase factor from the other hopping channel $T_{\Gamma, \mathbf{K}}^\dagger$, one finds that $\Delta_{\text{int}} \rightarrow \Delta_{\text{int}} e^{i\theta}$. Thus, the phase factor of the valley mixing can be manipulated by the direction of the Néel vector of MPX₃. In particular, MnPSe₃ is experimentally probed to be a candidate material of XY model where the direction of its Néel vector can be tuned by strain[36, 37], which makes the phase tuning of Δ_{int} experimentally feasible.

As every term in equation (1) has been determined from first principle, we calculate and obtain the moiré bands using the plane-wave basis[5] (see appendix). In Fig.4(a), we compare the moiré band structures with and without intervalley coupling. Without intervalley coupling, the moiré bands from \mathbf{K} and \mathbf{K}' valleys cross each other in between κ' and κ'_- . With intervalley coupling, the crossings are avoided and a local band gap of about 1 meV is formed. Near the avoided crossing, the valley components of the moiré bands transition from $\kappa(\kappa')$ component to $\kappa'(\kappa)$ component.

Without external magnetic field, however, the top two moiré bands are degenerate at γ due to a combined symmetry of time reversal and mirror (along three A-B-C paths generated by \hat{C}_3) in the moiré superlattices. To lift the degeneracy at γ , we apply an out-of-plane magnetic field to create a Zeeman splitting between the two valleys, i.e.

$$H_{\text{eff}}(\mathbf{r}) = \begin{bmatrix} H_{\mathbf{k}-\kappa} + V_d(\mathbf{r}) + E_g & \Delta_{\text{int}}(\mathbf{r}) \\ \Delta_{\text{int}}^\dagger(\mathbf{r}) & H_{\mathbf{k}+\kappa} + V_d(\mathbf{r}) - E_g \end{bmatrix}. \quad (4)$$

As Δ_{int} and E_g are fully tunable by electric and magnetic field, respectively, we explore the topological phases of the bands as these two parameters are tuned. We first check the band structure at $\Delta = -0.7$ meV and $E_g = 3.45$ meV. Under this parameter setting, the topmost moiré band becomes fully isolated as in Fig.4(b). We then calculate the Berry curvature and integrated it over the moiré Brillouin zone[38]. We find that the first band has a Chern number of 1, while the second band carries a Chern number of -1. The Berry

curvature is maximized around κ' where the band inversion occurs as in Fig.4(c). When the Fermi level is tuned between the two bands, this heterostructure becomes a Chern insulator with a band gap of about 0.1 meV.

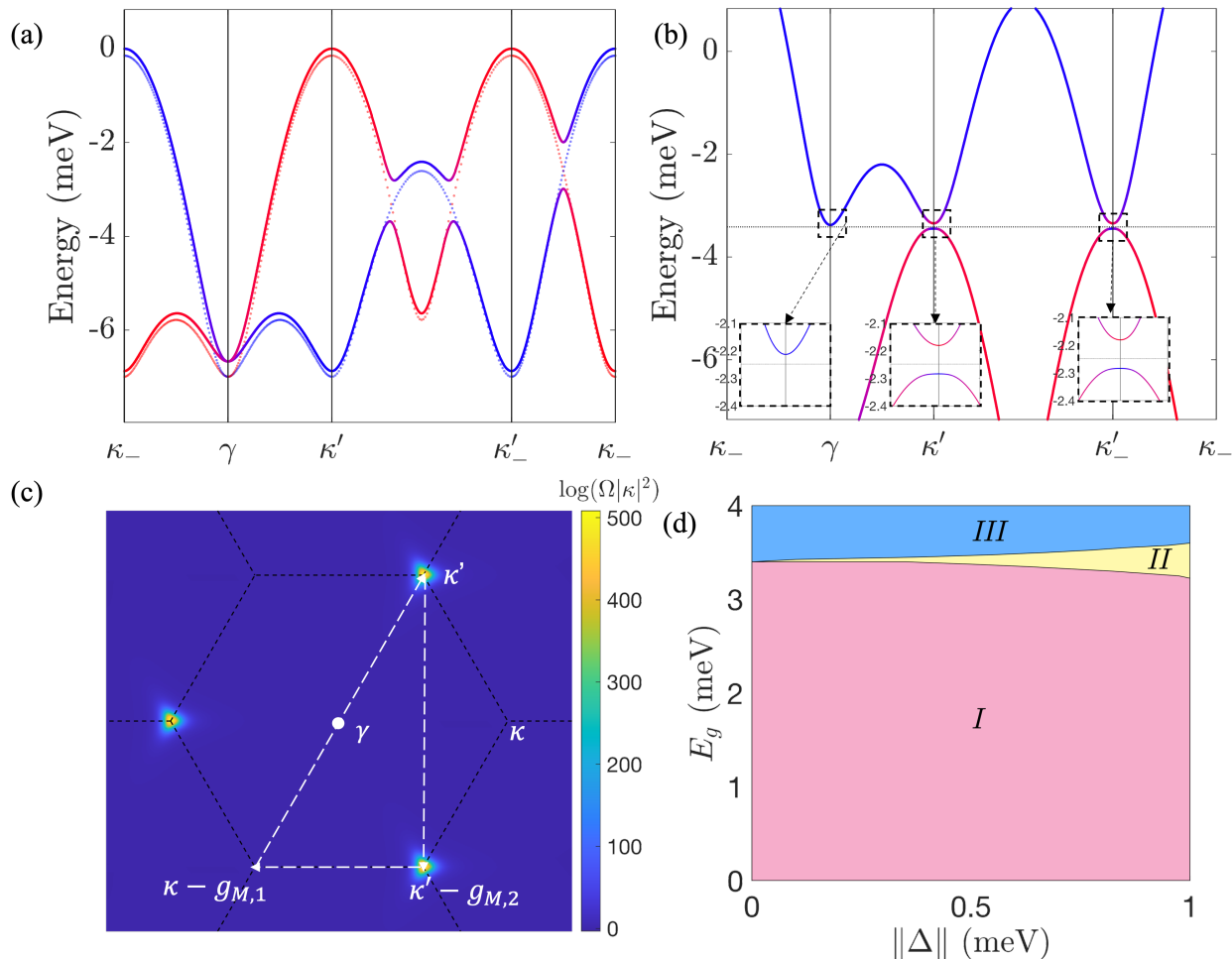


Figure 4: (a) Moiré bandstructure of MoTe₂/MnPSe₃. Blue(red) represents κ (κ') band. Solid(dashed) lines are bands with(without) intervalley coupling computed from equation(3). The topmost bands are degenerate at γ . (b) Same as (a) but with external displacement field and intervalley Zeeman splitting. When the Fermi level is tuned between the first and second band, the system becomes a Chern insulator. Insets show zoomed-in gaps. (c) Normalized Berry curvature over the moiré Brillouin zone decorated with the k-path for (a) and (b): $\kappa - g_{M,1}(\kappa_-) \rightarrow \gamma \rightarrow \kappa' \rightarrow \kappa' - g_{M,2}(\kappa'_-) \rightarrow \kappa - g_{M,1}(\kappa_-)$ (d) Phase diagram in the space spanned by E_g and $\|\Delta\|$. Region I (in red) denotes that the first two moiré bands are staggered with no global gap, and the Chern number of the first (second) band is 1 (-1). Region II (in yellow) denotes a quantum anomalous Hall insulator. Region III (in blue) denotes a band insulator.

As mentioned previously, an out-of-plane magnetic field can break the combined time reversal and mirror symmetry. However, to reach the desired Zeeman splitting of about 3.5 meV for the Chern insulator phase, a magnetic field of 10 T is required, even considering the large g -factor of the MoTe₂ valleys[39–41]. This challenge can be resolved in two ways. First, we can cap MoTe₂/MnPSe₃ using another easy axis vdW magnet, e.g. CrBr₃, which can create valley splittings as large as 10 meV[28]. Second, an out-of-plane magnetic field can cant the magnetic moments in MnPSe₃ along the z -direction, and the proximity effect

would induce a large effective Zeeman splitting in the MoTe₂ valleys.

The highly tunable pseudospin textures allow us to control the topological phases of the Kekulé moiré superlattices as a function Δ and E_g (Fig.4(d)). In region *I*, under small E_g , the top two moiré bands are staggered and a global gap is absent, but the Chern number can be readily computed to be 1(−1) for the first (second) band. With increasing E_g , a global gap appears between the first and second band in region *II*. Since no band crossing happens yet, these bands remain topologically non-trivial. In this region, for one hole doping per moiré supercell, the system is in the Chern insulator phase as exemplified by Fig.4(b). At even higher E_g , the band gap closes, and after which trivial insulator phase kicks in at region *III*. As Δ increases, the allowed range of E_g to realize the Chern insulator phases and the topological gap of the Chern insulator both increase. As the topological gap in the Kekulé moiré superlattice arises from intervalley coupling mediated by the magnetic substrate, such gap can survive even at temperatures much larger than the gap size, as long as the magnetic order stays.

3 Summary

We have introduced a new type of moiré materials, where the lattices of the two constituent layers are related by a Kekulé reconstruction. Using MoTe₂/MnPSe₃ as an example, we have shown that the magnetism in MnPSe₃ enables the coupling between the Kramers' valley-spin states in MoTe₂. Lastly, we have constructed the effective moiré Hamiltonian, and show that the fascinating valley-pseudospin texture and non-trivial band topology can be tuned on-demand. The ability to fully control the Kramers' valley-spin pairs could provide a new basis to enrich the moiré playground for quantum information science and materials research.

4 Appendix

4.1 First Principle Calculations

In the first-principles calculations of the 12×12 commensurate structures based on local stacking geometry in the moiré supercell, we use the lattice constant $\sqrt{3}a_{\text{MoTe}_2} = 6.11 \text{ \AA}$ based on $a_{\text{MoTe}_2} = 3.53 \text{ \AA}$ obtained from relaxation. We use Perdew-Burke-Ernzerhof (PBE)[42] for the exchange-correlation functional as implemented in Vienna *ab initio* simulation package (VASP)[43]. We employ projector augmented wave (PAW) pseudopotentials[44] with a plane-wave energy cutoff for the wavefunctions of 500 eV. The k -mesh is set to 9×9 and centered around Γ . The internal atomic coordinates are fully relaxed until the force on every atom is small than 0.02 eV/\AA . Van der Waals interactions are included within the DFT-D2 framework[45]. We set the vacuum thickness to be 18 \AA to avoid interactions between repeated images. For the self-consistent calculation, a fully relativistic calculation is performed to include spin-orbit coupling. To accurately capture the magnetism of MnPSe₃, we apply the GGA plus on-site Hubbard U method (GGA+U)[46] where U is set to 4 eV for the Mn ions similar to previous calculations[47]. We note that the DFT calculations usually underestimate the quasiparticle bandgap, compared to the GW calculations which are extremely high in computational cost in this heterostructure. However, the physics demonstrated in our work does not rely on the absolute value of the band gap. The important intervalley coupling arising from the magnetic substrate would not be affected, because such couplings act on degenerate valleys with the same quasiparticle self-energy correction.

4.2 Moiré Lattice Vector

In Kekulé moiré superlattices, the lattice constants of the larger (smaller) lattice are denoted as $\{\mathbf{a}_{L,1}, \mathbf{a}_{L,2}\}$ ($\{\mathbf{a}_{S,1}, \mathbf{a}_{S,2}\}$), and their directions can be referred to the inset of Fig. 1(a). The superlattice formed by stacking two hexagonal lattice is also hexagonal. However, the moiré superlattice constant extracted based on the reconstructed Kekulé cell using the common continuum formula, i.e., $L_M = \frac{a_L}{\sqrt{\delta^2 + \theta^2}}$, is off from the true value by $\sqrt{3}$. Here,

$\delta \equiv \frac{|a_L - \sqrt{3}a_S|}{a_L}$ and θ is measured from the 30° angle. This discrepancy can be solved from carefully analyzing the displacement vector. When we start from a lattice point, and travel by $u\mathbf{a}_{L,1} + v\mathbf{a}_{L,2}$, this point is off from the lattice point at $u(\mathbf{a}_{S,1} + \mathbf{a}_{S,2}) + v(2\mathbf{a}_{L,1} - \mathbf{a}_{S,2})$ by the displacement vector, $\mathbf{d}(u, v)$. Explicitly, the displacement vector reads

$$\mathbf{d}(u, v) = \delta(u\mathbf{a}_{L,1} + v\mathbf{a}_{L,2}).$$

When we transverse to a certain (u, v) , if $\mathbf{d}(u, v)$ is equal to some integer combination of $\{\mathbf{a}_{L,1}, \mathbf{a}_{L,2}\}$, then the lattice points of the larger lattice and the smaller lattice at $u\mathbf{a}_{L,1} + v\mathbf{a}_{L,2}$ should overlap. This is exactly a periodicity at the wavelength of $u\mathbf{a}_{L,1} + v\mathbf{a}_{L,2}$. The true moiré periodicity should happen with $\mathbf{d}(u, v)$ equal to exactly one unit cell lattice constant.

If we try $\mathbf{d}(u, v) = \mathbf{a}_{L,1}$, we get $u = \frac{1}{\delta}$, and $L_M = \|u\hat{\mathbf{a}}_{L,1}\| = \frac{a_L}{\delta}$, which is still the value that is off by a factor of $\sqrt{3}$. The remedy comes from the fact that the smallest unit cell lattice constant is actually \mathbf{a}_S . When $\mathbf{d}(u, v) = \mathbf{a}_{S,1}$, $u = v = \frac{a_S}{\sqrt{3}\delta}$, and $L_M = \|u\hat{\mathbf{a}}_{L,1} + v\hat{\mathbf{a}}_{L,2}\| = \frac{a_S}{\delta}$. Indeed, to construct the smallest moiré period, the displacement vector is equal to one primitive lattice vector of TMD, which in turn ensures that the primitive lattice vectors of the moiré lattice are parallel to those of the TMD. Combining with a twist angle, the true moiré period is given by

$$L_M = \frac{a_S}{\sqrt{\delta^2 + \theta^2}}. \quad (5)$$

At small lattice mismatch/twist angle, the continuum model is usually constructed with locally commensurate structure, and each local structure can be constructed by displacing one unit cell relative to another. The conventional real space moiré unit cell is then fully captured when the displacement vector scans the unit cell of the commensurate structure. In the case of Kekulé moiré, the displacement vector only needs to scan the unit cell of the TMD, which is one third of the area of the locally commensurate unit cell.

4.3 Microscopic Theory of Effective Intervalley Coupling

In the main text, we used first-principles calculations to obtain the off-diagonal parts of the moiré Hamiltonian. Alternatively, The interlayer hopping matrix can be computed from the two-center approximation[1, 3, 35]. We first write down the sublattice resolved plane wave basis for TMD centered around $\pm\mathbf{K}$ and MPX₃ centered around Γ as

$$|\psi_{n,\eta\mathbf{K}+\mathbf{k}}^{\alpha,S}(\mathbf{r})\rangle = \frac{1}{\sqrt{N}} \sum_{\mathbf{R}} e^{i(\eta\mathbf{K}+\mathbf{k})\cdot(\mathbf{R}+\tau_\alpha)} |n(\mathbf{r} - \mathbf{R} - \tau_\alpha)\rangle \otimes |\sigma_\eta\rangle, \quad (6)$$

$$|\psi_{m,\Gamma+\mathbf{k}'}^{\beta,L}(\mathbf{r})\rangle = \frac{1}{\sqrt{N'}} \sum_{\mathbf{R}'} e^{i(\Gamma+\mathbf{k}')\cdot(\mathbf{R}'+\tau_\beta)} |m(\mathbf{r} - \mathbf{R}' - \tau_\beta)\rangle \otimes |\sigma_\beta\rangle. \quad (7)$$

S (L), α (β), $\boldsymbol{\tau}_\alpha$ ($\boldsymbol{\tau}_\beta$), n (m), N (N'), \mathbf{R} (\mathbf{R}'), \mathbf{k} (\mathbf{k}') denote the smaller (larger) lattice, sublattice indices, sublattice coordinates, band indices, number of unit cells, lattice vectors, crystal momenta of TMD(MPX₃) respectively. $\eta = \pm$ denotes the valley degree of freedom. The wavefunctions can be decomposed into two parts: the local orbital part $|n\rangle$ ($|m\rangle$) and the spinor part $|\sigma_\eta\rangle$ ($|\sigma_\beta\rangle$). Notably, for TMD the spinor part depends on the valley index η , while for MPX₃ the spinor part depends on the sublattice index. The hopping channel can be then expressed as

$$\begin{aligned} T_{\Gamma \rightarrow \eta \mathbf{K}}^{\alpha, \beta} &\equiv \langle \psi_{n, \eta \mathbf{K} + \mathbf{k}}^{\alpha, S}(\mathbf{r}) | \psi_{m, \Gamma + \mathbf{k}'}^{\beta, L}(\mathbf{r}) \rangle \\ &= \frac{1}{\sqrt{NN'}} \sum_{\mathbf{R}, \mathbf{R}'} e^{-i(\eta \mathbf{K} + \mathbf{k}) \cdot (\mathbf{R} + \boldsymbol{\tau}_\alpha) + i\mathbf{k}' \cdot (\mathbf{R}' + \boldsymbol{\tau}_\beta)} \\ &\quad \times \langle n(\mathbf{r} - \mathbf{R} - \boldsymbol{\tau}_\alpha) | m(\mathbf{r} - \mathbf{R}' - \boldsymbol{\tau}_\beta) \rangle \times \langle \sigma_\eta | \sigma_\beta \rangle. \end{aligned}$$

The two-center approximation takes $\langle n(\mathbf{r} - \mathbf{R} - \boldsymbol{\tau}_\alpha) | m(\mathbf{r} - \mathbf{R}' - \boldsymbol{\tau}_\beta) \rangle$ as $t_{nm}(\mathbf{R} + \boldsymbol{\tau}_\alpha - \mathbf{R}' - \boldsymbol{\tau}_\beta)$. Then after Fourier transform, we arrive at the final expression:

$$\begin{aligned} T_{\Gamma \rightarrow \eta \mathbf{K}}^{\alpha, \beta} &= \frac{1}{\sqrt{\Omega \Omega'}} \sum_{\mathbf{G}_S, \mathbf{G}_L} \delta_{\eta \mathbf{K} + \mathbf{k} + \mathbf{G}_S, \mathbf{k}' + \mathbf{G}_L} t_{nm}(\eta \mathbf{K} + \mathbf{k} + \mathbf{G}_S) \\ &\quad \times e^{i\mathbf{G}_S \cdot \boldsymbol{\tau}_\alpha} e^{-i\mathbf{G}_L \cdot \boldsymbol{\tau}_\beta} \langle \sigma_\eta | \sigma_\beta \rangle. \end{aligned}$$

Here, Ω (Ω') is the unit cell area of TMD (MPX₃); \mathbf{G}_S (\mathbf{G}_L) is the reciprocal lattices of TMD (MPX₃); $t_{nm}(\mathbf{q})$ is the Fourier transformed amplitude of $t_{nm}(\mathbf{r})$. The full hopping channel matrix is obtained by identifying the sublattice indices α, β as matrix indices. For example, in MoTe₂/MnPSe₃, $T_{\Gamma \rightarrow \eta \mathbf{K}}$ will be a 3×2 matrix as it considers a hopping from two magnetic Mn ions to three Mo ions.

The real space Hamiltonian in this formalism reads:

$$H(\mathbf{r}) = \begin{bmatrix} H_\Gamma(\mathbf{r}) & T_{\Gamma \rightarrow \mathbf{K}}^\dagger & T_{\Gamma \rightarrow \mathbf{K}'}^\dagger \\ T_{\Gamma \rightarrow \mathbf{K}} & H_\mathbf{K}(\mathbf{r}) & 0 \\ T_{\Gamma \rightarrow \mathbf{K}'} & 0 & H_{\mathbf{K}'}(\mathbf{r}) \end{bmatrix}.$$

Note that each matrix element is by itself a matrix. In MoTe₂/MnPSe₃ Kekulé moiré, H_Γ is a 2×2 matrix, while $H_\mathbf{K}(\mathbf{r})$ is a 3×3 matrix. These diagonal matrix elements denote the standalone monolayer Hamiltonians. The intervalley coupling effect can then be obtained using a downfolding technique:

$$H_{\text{eff}}(\mathbf{r}) = \begin{bmatrix} H_\mathbf{K} + C_{\mathbf{K}\mathbf{K}} \times \frac{1}{2} T_{\Gamma \rightarrow \mathbf{K}} T_{\Gamma \rightarrow \mathbf{K}}^\dagger & C_{\mathbf{K}\mathbf{K}'} \times \frac{1}{2} T_{\Gamma \rightarrow \mathbf{K}} T_{\Gamma \rightarrow \mathbf{K}'}^\dagger \\ C_{\mathbf{K}'\mathbf{K}} \times \frac{1}{2} T_{\Gamma \rightarrow \mathbf{K}} T_{\Gamma \rightarrow \mathbf{K}'}^\dagger & H_{\mathbf{K}'} + C_{\mathbf{K}'\mathbf{K}'} \times \frac{1}{2} T_{\Gamma \rightarrow \mathbf{K}'} T_{\Gamma \rightarrow \mathbf{K}'}^\dagger \end{bmatrix},$$

$$C_{\eta \mathbf{K}, \eta' \mathbf{K}} = \left(\frac{1}{H_{\eta \mathbf{K}} - H_\Gamma} + \frac{1}{H_{\eta' \mathbf{K}} - H_\Gamma} \right).$$

We recognize that the two-step hopping would provide both the diagonal and off-diagonal moiré potential (V_d and Δ_{int}). However, there's a caveat to it as this formalism treats the two layers as rigid bodies, i.e. there's no corrugation effects. As a result, it would predict that V_d and Δ_{int} are on the same order of magnitude, while DFT calculation (which includes corrugation effects) predicts V_d to be about one order of magnitude larger than Δ_{int} .

4.4 Intervalley Coupling Selection Rule

Since $T_{\Gamma, \pm \mathbf{K}}$ depend on the magnetic order in MPX_3 as well as the local stackings, under some configurations Δ_{int} vanishes by symmetry. For example, as shown in the main text, the out-of-plane magnetic orders are not capable of connecting $|\pm \mathbf{K}\rangle$ because the spinor product in one of $T_{\Gamma, \pm \mathbf{K}}$ becomes zero. We then notice that to lift the degeneracy of the $|\mathbf{K}\rangle - |\mathbf{K}'\rangle$ Kramers' pair, the time reversal symmetry, $\hat{\mathcal{T}}$, needs to be broken, where this condition is indeed fulfilled in all AFM orders. However, the time reversal with a sublattice translation is still a symmetry for some of the AFM orders. Notably, the AFM stripy phase and zigzag phase are invariant under $\hat{\mathcal{T}}\hat{\tau}_{\mathbf{a}_{\text{MPX}_3, 2/2}}$, where $\mathbf{a}_{\text{MPX}_3, 2}$ is the lattice vector in the $(\frac{1}{2}, \frac{\sqrt{3}}{2})$ direction. In the Bloch wave representation, $\hat{\tau}_{\mathbf{a}_{\text{MPX}_3, 2/2}}$ becomes a phase factor, thus $\hat{\mathcal{T}}\hat{\tau}_{\mathbf{a}_{\text{MPX}_3, 2/2}}|\mathbf{K}\rangle$ still maps to $|\mathbf{K}'\rangle$ up to a phase factor. In other words, $|\mathbf{K}\rangle$ and $|\mathbf{K}'\rangle$ still form an effective Kramers' pair, and the degeneracy is intact. For Néel AFM order, however, no such symmetry as $\hat{\mathcal{T}}\hat{\tau}_{\mathbf{a}_{\text{MPX}_3, 2/2}}$ is present. As a result, we conclude that Δ_{int} can only occur in in-plane Néel AFM and FM orders.

4.5 Plane Wave Basis Method

As the moiré Hamiltonian is translational invariant under \mathbf{a}_M , we can diagonalize the moiré Hamiltonian using the moiré wavevector basis, $\{|\mathbf{k} - \eta\boldsymbol{\kappa} + \mathbf{g}_M\rangle\}$, where $\eta = \pm 1$ denotes the two different valleys and \mathbf{g}_M is a moiré reciprocal lattice vector [5]. For the diagonal terms, the non-zero matrix elements are the ones from the same valley

$$\begin{aligned}\langle \mathbf{k} - \boldsymbol{\kappa} + \mathbf{g}_M | H_{\mathbf{k} - \boldsymbol{\kappa}} | \mathbf{k} - \boldsymbol{\kappa} + \mathbf{g}'_M \rangle &= -\delta_{\mathbf{g}_M, \mathbf{g}'_M} \frac{\hbar^2 (\mathbf{k} - \boldsymbol{\kappa})^2}{2m^*}, \\ \langle \mathbf{k} + \boldsymbol{\kappa} + \mathbf{g}_M | H_{\mathbf{k} + \boldsymbol{\kappa}} | \mathbf{k} + \boldsymbol{\kappa} + \mathbf{g}'_M \rangle &= -\delta_{\mathbf{g}_M, \mathbf{g}'_M} \frac{\hbar^2 (\mathbf{k} + \boldsymbol{\kappa})^2}{2m^*}, \\ \langle \mathbf{k} - \eta\boldsymbol{\kappa} + \mathbf{g}_M | V_d | \mathbf{k} - \eta\boldsymbol{\kappa} + \mathbf{g}'_M \rangle &= V_d(\mathbf{g}_M - \mathbf{g}'_M).\end{aligned}$$

Here, $V_d(\mathbf{g}_M - \mathbf{g}'_M)$ is the Fourier transformed $V_d(\mathbf{r})$. Similarly, for the off-diagonal terms, the matrix element is only non-zero between states from different valleys:

$$\begin{aligned}\langle \mathbf{k} - \boldsymbol{\kappa} + \mathbf{g}_M | \Delta_{\text{int}} | \mathbf{k} + \boldsymbol{\kappa} + \mathbf{g}'_M \rangle &= \Delta_{\text{int}}(\mathbf{g}_M - \mathbf{g}'_M), \\ \langle \mathbf{k} + \boldsymbol{\kappa} + \mathbf{g}_M | \Delta_{\text{int}}^\dagger | \mathbf{k} - \boldsymbol{\kappa} + \mathbf{g}'_M \rangle &= \Delta_{\text{int}}^*(\mathbf{g}_M - \mathbf{g}'_M).\end{aligned}$$

Again, $\Delta_{\text{int}}(\mathbf{g}_M - \mathbf{g}'_M)$ is nothing but the Fourier transformed $\Delta_{\text{int}}(\mathbf{r})$.

With knowing these matrix elements, one can write down the moiré Hamiltonian and the basis set in the \mathbf{k} -space with any number of Brillouin zones. In this work, the calculation is carried out with 7×7 moiré Brillouin zone to reduce the finite size errors for the first few moiré bands.

Acknowledgments

The first-principles calculations of two-dimensional magnetic materials was supported by the University of Washington Molecular Engineering Materials Center (DMR-1719797). The theoretical study of Kekulé moiré Hamiltonian is supported by the Department of Energy BES QIS program on 'Van der Waals Reprogrammable Quantum Simulator' under award number DE-SC0022277. This work was facilitated through the use of advanced computational, storage, and networking infrastructure provided by the Hyak supercomputer system and funded

by the University of Washington Molecular Engineering Materials Center at the University of Washington.

References

- [1] R. Bistritzer and A. H. MacDonald, Proceedings of the National Academy of Sciences **108**, 12233 (2011).
- [2] S. Shallcross, S. Sharma, E. Kandelaki, and O. Pankratov, Physical Review B **81**, 165105 (2010).
- [3] F. Wu, T. Lovorn, E. Tutuc, I. Martin, and A. MacDonald, Physical review letters **122**, 086402 (2019).
- [4] Y. Zhang, T. Devakul, and L. Fu, Proceedings of the National Academy of Sciences **118**, e2112673118 (2021).
- [5] F. Wu, T. Lovorn, E. Tutuc, and A. H. MacDonald, Physical review letters **121**, 026402 (2018).
- [6] Y. Tang, L. Li, T. Li, Y. Xu, S. Liu, K. Barmak, K. Watanabe, T. Taniguchi, A. H. MacDonald, J. Shan, et al., Nature **579**, 353 (2020).
- [7] Y. Cao, V. Fatemi, A. Demir, S. Fang, S. L. Tomarken, J. Y. Luo, J. D. Sanchez-Yamagishi, K. Watanabe, T. Taniguchi, E. Kaxiras, et al., Nature **556**, 80 (2018).
- [8] Y. Cao, V. Fatemi, S. Fang, K. Watanabe, T. Taniguchi, E. Kaxiras, and P. Jarillo-Herrero, Nature **556**, 43 (2018).
- [9] T. Li, S. Jiang, B. Shen, Y. Zhang, L. Li, Z. Tao, T. Devakul, K. Watanabe, T. Taniguchi, L. Fu, et al., Nature **600**, 641 (2021).
- [10] P. Wang, G. Yu, Y. H. Kwan, Y. Jia, S. Lei, S. Klemenz, F. A. Cevallos, R. Singha, T. Devakul, K. Watanabe, et al., Nature **605**, 57 (2022).
- [11] B. Hunt, J. D. Sanchez-Yamagishi, A. F. Young, M. Yankowitz, B. J. LeRoy, K. Watanabe, T. Taniguchi, P. Moon, M. Koshino, P. Jarillo-Herrero, et al., Science **340**, 1427 (2013).
- [12] E. C. Regan, D. Wang, C. Jin, M. I. Bakti Utama, B. Gao, X. Wei, S. Zhao, W. Zhao, Z. Zhang, K. Yumigeta, et al., Nature **579**, 359 (2020).
- [13] K. L. Seyler, P. Rivera, H. Yu, N. P. Wilson, E. L. Ray, D. G. Mandrus, J. Yan, W. Yao, and X. Xu, Nature **567**, 66 (2019).
- [14] X. Xu, W. Yao, D. Xiao, and T. F. Heinz, Nature Physics **10**, 343 (2014).
- [15] C. Gutiérrez, C.-J. Kim, L. Brown, T. Schiros, D. Nordlund, E. B. Lochocki, K. M. Shen, J. Park, and A. N. Pasupathy, Nature Physics **12**, 950 (2016).
- [16] S. Ryu, C. Mudry, C.-Y. Hou, and C. Chamon, Physical Review B **80**, 205319 (2009).
- [17] C.-Y. Hou, C. Chamon, and C. Mudry, Physical review letters **98**, 186809 (2007).
- [18] G.-B. Liu, H. Pang, Y. Yao, and W. Yao, New Journal of Physics **16**, 105011 (2014).
- [19] C. Bao, H. Zhang, T. Zhang, X. Wu, L. Luo, S. Zhou, Q. Li, Y. Hou, W. Yao, L. Liu, et al., Physical Review Letters **126**, 206804 (2021).
- [20] X. Liu, G. Farahi, C.-L. Chiu, Z. Papic, K. Watanabe, T. Taniguchi, M. P. Zaletel, and A. Yazdani, Science **375**, 321 (2022).

- [21] N. Bultinck, E. Khalaf, S. Liu, S. Chatterjee, A. Vishwanath, and M. P. Zaletel, *Physical Review X* **10**, 031034 (2020).
- [22] D. Xiao, G.-B. Liu, W. Feng, X. Xu, and W. Yao, *Physical review letters* **108**, 196802 (2012).
- [23] T. Cao, G. Wang, W. Han, H. Ye, C. Zhu, J. Shi, Q. Niu, P. Tan, E. Wang, B. Liu, et al., *Nature communications* **3**, 1 (2012).
- [24] N. Sivadas, M. W. Daniels, R. H. Swendsen, S. Okamoto, and D. Xiao, *Physical Review B* **91**, 235425 (2015).
- [25] B. L. Chittari, Y. Park, D. Lee, M. Han, A. H. MacDonald, E. Hwang, and J. Jung, *Physical Review B* **94**, 184428 (2016).
- [26] K. L. Seyler, D. Zhong, B. Huang, X. Linpeng, N. P. Wilson, T. Taniguchi, K. Watanabe, W. Yao, D. Xiao, M. A. McGuire, et al., *Nano letters* **18**, 3823 (2018).
- [27] M. Onga, Y. Sugita, T. Ideue, Y. Nakagawa, R. Suzuki, Y. Motome, and Y. Iwasa, *Nano Letters* **20**, 4625 (2020).
- [28] H. Zhang, W. Yang, Y. Ning, and X. Xu, *Physical Review B* **101**, 205404 (2020).
- [29] C. Zhao, T. Norden, P. Zhang, P. Zhao, Y. Cheng, F. Sun, J. P. Parry, P. Taheri, J. Wang, Y. Yang, et al., *Nature nanotechnology* **12**, 757 (2017).
- [30] B. Scharf, G. Xu, A. Matos-Abiague, and I. Žutić, *Physical review letters* **119**, 127403 (2017).
- [31] G. Ouvrard, R. Brec, and J. Rouxel, *Materials research bulletin* **20**, 1181 (1985).
- [32] P. Joy and S. Vasudevan, *Physical Review B* **46**, 5425 (1992).
- [33] G. Le Flem, R. Brec, G. Ouvard, A. Louisy, and P. Segransan, *Journal of Physics and Chemistry of Solids* **43**, 455 (1982).
- [34] A. Wildes, V. Simonet, E. Ressouche, R. Ballou, and G. McIntyre, *Journal of Physics: Condensed Matter* **29**, 455801 (2017).
- [35] Y. Wang, Z. Wang, W. Yao, G.-B. Liu, and H. Yu, *Physical Review B* **95**, 115429 (2017).
- [36] Z. Ni, A. Haglund, H. Wang, B. Xu, C. Bernhard, D. Mandrus, X. Qian, E. Mele, C. Kane, and L. Wu, *Nature Nanotechnology* **16**, 782 (2021).
- [37] P. Jeevanandam and S. Vasudevan, *Journal of Physics: Condensed Matter* **11**, 3563 (1999).
- [38] D. Xiao, M.-C. Chang, and Q. Niu, *Reviews of modern physics* **82**, 1959 (2010).
- [39] G. Aivazian, Z. Gong, A. M. Jones, R.-L. Chu, J. Yan, D. G. Mandrus, C. Zhang, D. Cobden, W. Yao, and X. Xu, *Nature Physics* **11**, 148 (2015).
- [40] T. Deilmann, P. Krüger, and M. Rohlfing, *Physical review letters* **124**, 226402 (2020).
- [41] C. Robert, H. Dery, L. Ren, D. Van Tuan, E. Courtade, M. Yang, B. Urbaszek, D. Lagarde, K. Watanabe, T. Taniguchi, et al., *Physical Review Letters* **126**, 067403 (2021).
- [42] J. P. Perdew, K. Burke, and M. Ernzerhof, *Physical review letters* **77**, 3865 (1996).
- [43] G. Kresse and J. Furthmüller, *Computational materials science* **6**, 15 (1996).
- [44] G. Kresse and D. Joubert, *Physical review b* **59**, 1758 (1999).
- [45] S. Grimme, *Journal of computational chemistry* **27**, 1787 (2006).

- [46] A. Liechtenstein, V. I. Anisimov, and J. Zaanen, *Physical Review B* **52**, R5467 (1995).
- [47] L. Wang, T. Maxisch, and G. Ceder, *Physical Review B* **73**, 195107 (2006).